Supplementary Materials: Thermoelectric Properties of *Pnma* and Rocksalt SnS and SnSe

Joseph M. Flitroft, Ioanna Pallikara and Jonathan M. Skelton

Table S1. Comparison of the optimised lattice parameters of *Pnma* SnS and SnSe obtained in this work to the study in [1]. Note that the axes in [1] have been relabelled to match the orientation of the unit cells in this work.

		a (Å)	b (Å)	c (Å)	V (Å^3)
SnS (*Pnma*)	This work	11.000	3.965	4.202	183.2
	Ref. [1]	11.143	3.971	4.336	192
	Δ [%]	-1.28	-0.15	-3.09	-4.58
SnSe (*Pnma*)	This work	11.350	4.124	4.335	202.9
	Ref. [1]	11.501	4.153	4.445	212
	Δ [%]	-1.31	-0.70	-2.47	-4.29

Table S2. Predicted maximum thermoelectric figures of merit ZT for the five systems examined in this work with the κ_{el} calculated using the Wiedemann-Franz law in Eq. 12 in the text. For each system we list the carrier concentration n and temperature T at which the maximum ZT is obtained together with the properties from Eq. 1 in the manuscript, namely the electrical conductivity σ, the Seebeck coefficient S, the power factor $S^2\sigma$ (PF), the electronic and lattice contributions to the thermal conductivity $\kappa_{el}/\kappa_{latt}$ and the total thermal conductivity κ_{tot}. These values may be compared to the data in Table 3 in the manuscript.

	n (cm^{-3})	T (K)	ZT	σ (S cm^{-1})	S (μV K^{-1})	PF $S^2\sigma$ (mW m^{-1} K^{-2})	κ (W m^{-1} K^{-1})		
							κ_{el}	κ_{latt}	κ_{tot}
SnS (*Pnma*)	3.16×10^{19}	1000	1.50	177	302	1.62	0.30	0.64	0.94
SnS (RS, Eq.)	6.81×10^{19}	820	2.81	539	326	5.73	1.54	0.49	2.03
SnS (RS, Comp.)	10^{20}	940	1.56	866	299	7.74	3.14	2.51	5.65
SnSe (*Pnma*)	2.15×10^{19}	1000	2.13	168	334	1.88	0.26	0.47	0.74
SnSe (RS)	10^{20}	940	2.33	1006	303	9.22	2.62	1.33	3.96

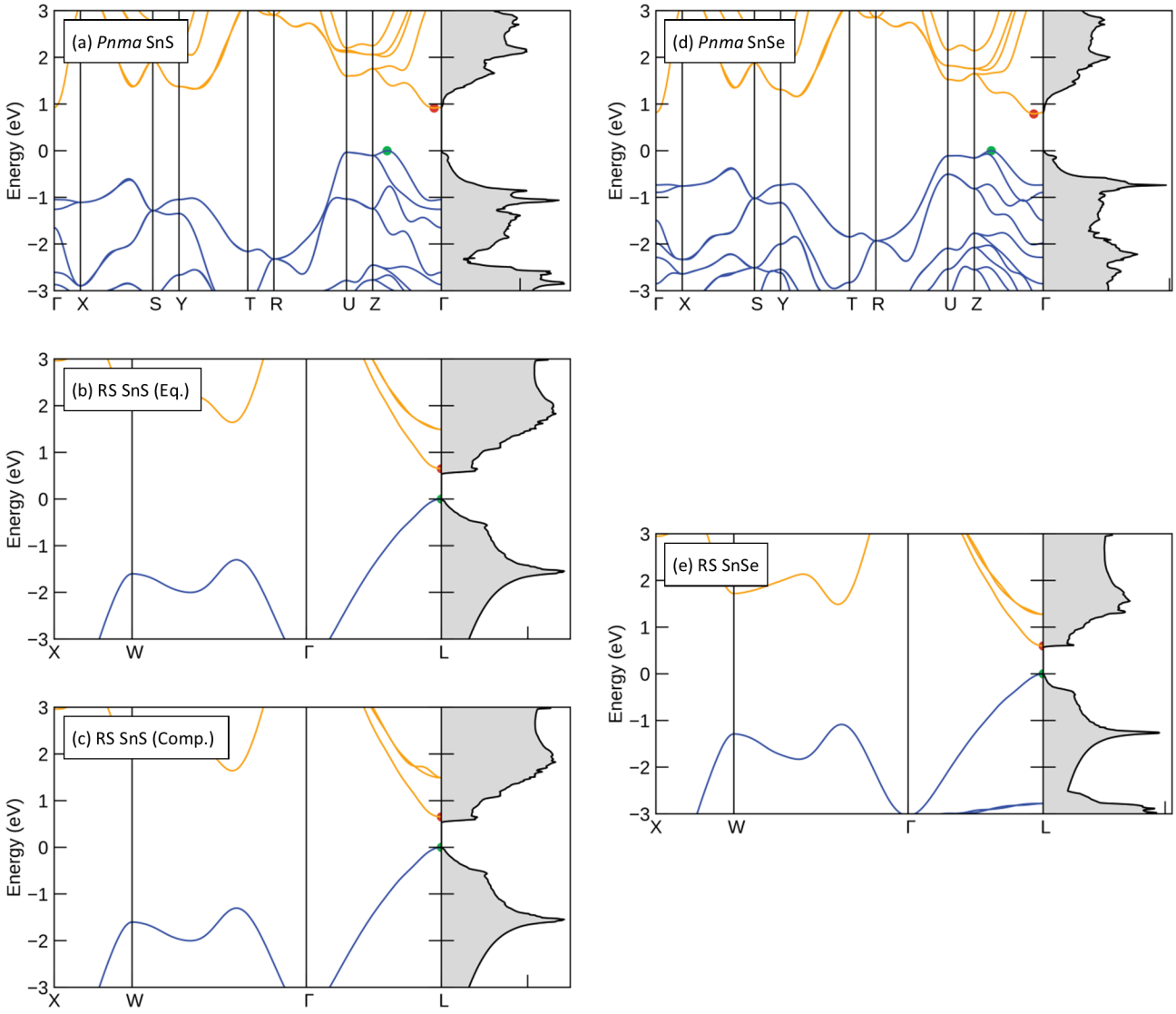

Figure S1. Calculated electronic band dispersion and density of states (DoS) of *Pnma* SnS (a), equilibrium/compressed rocksalt (RS) SnS (b/c), *Pnma* SnSe (d) and RS SnSe (e). On each dispersion the valence and conduction bands are shown in blue and yellow, respectively, and the valence-band maximum and conduction-band minimum (VBM/CBM) are marked by green and red circles. On each plot the VBM is set to 0 eV

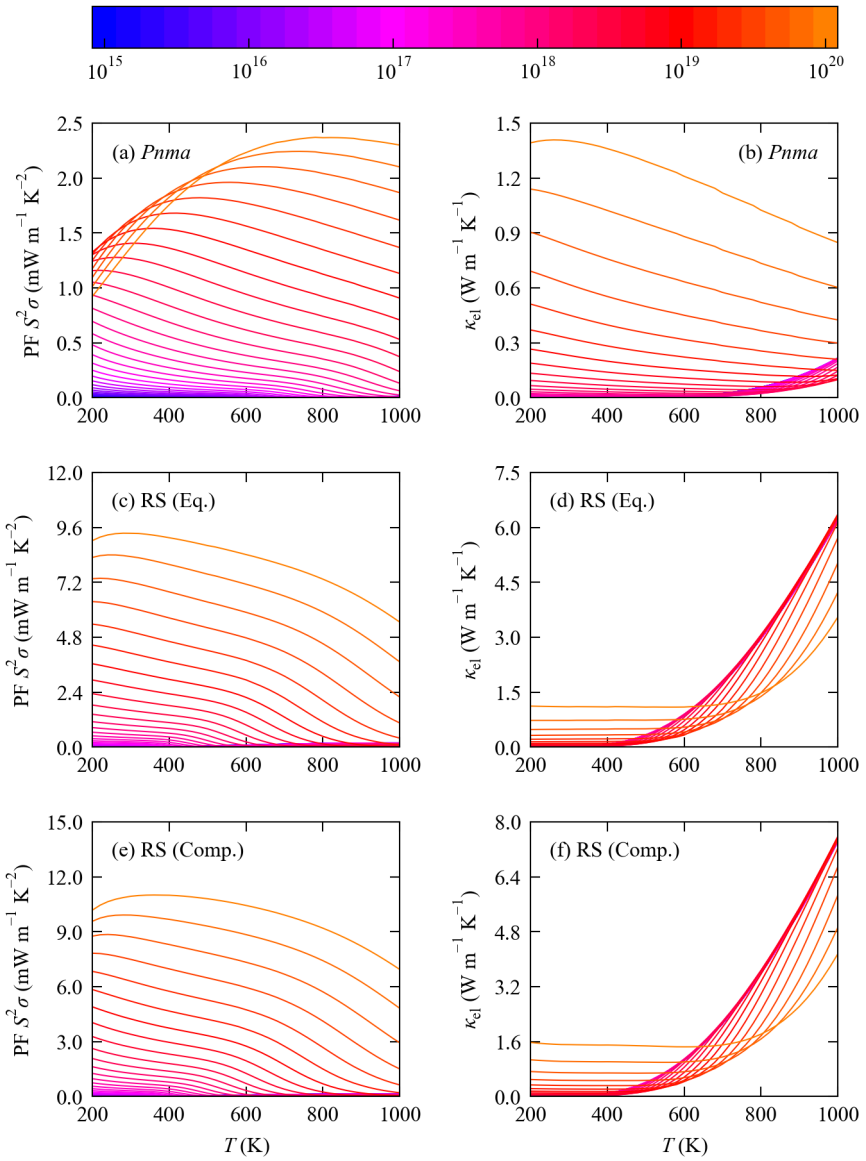

Figure S2. Calculated power factor $S^2\sigma$ (PF; a, c, e) and electronic thermal conductivity κ_{el} (b, d, f) of *Pnma* (a/b) and equilibrium/compressed rocksalt SnS (RS; Eq. - c/d; Comp. - e/f). The transport properties are shown as a function of temperature for carrier concentrations n from 10^{15}-10^{20} cm^{-3}, denoted by line colours from blue (small n) to orange (large n).

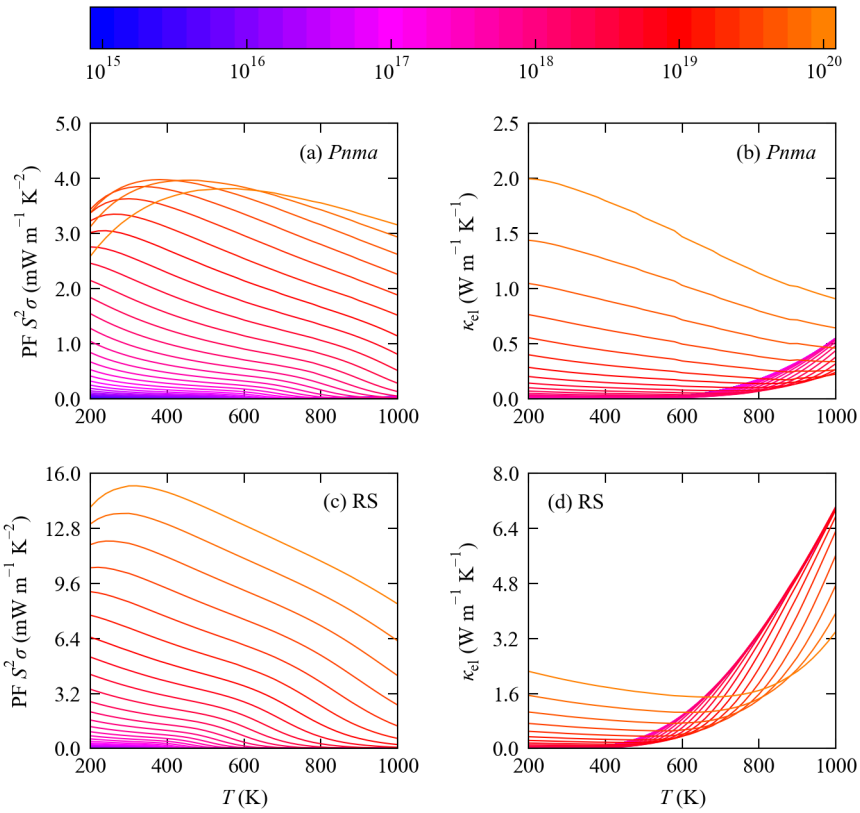

Figure S3. Calculated power factor $S^2\sigma$ (PF; a/c) and electronic thermal conductivity κ_{el} (b/d) of *Pnma* (a/b) and rocksalt (RS) SnSe (c/d). The transport properties are shown as a function of temperature for carrier concentrations n from 10^{15}-10^{20} cm^{-3}, denoted by line colours from blue (small n) to orange (large n).

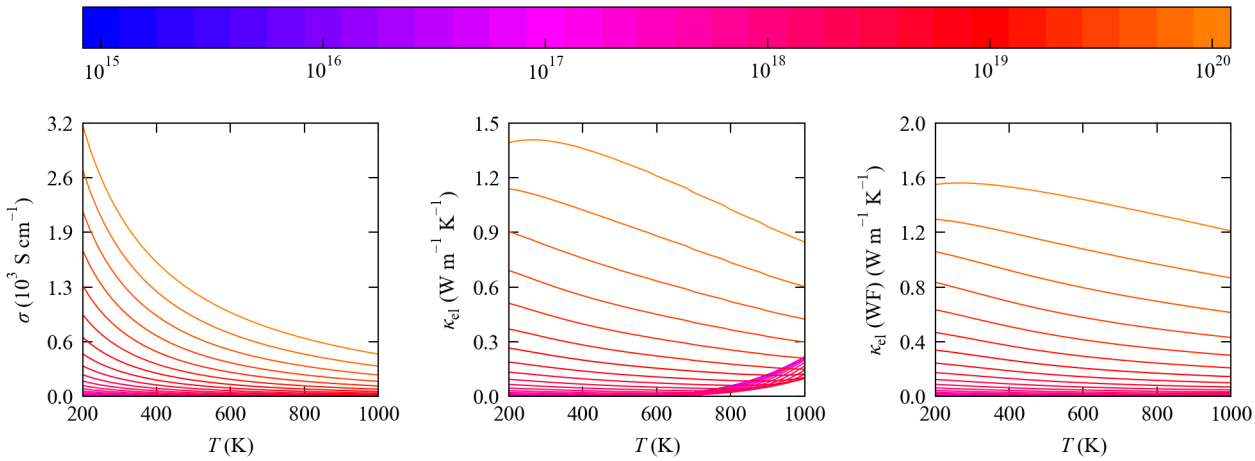

Figure S4. Comparison of the electrical conductivity σ of *Pnma* SnS with the electronic thermal conductivity κ_{el} computed using Eq. 7 in the manuscript and from the Weidemann-Franz law in Eq. 12. In each subplot the σ/κ_{el} are shown as a function of temperature for carrier concentrations n from 10^{15}-10^{20} cm^{-3}, denoted by line colours from blue (small n) to orange (large n).

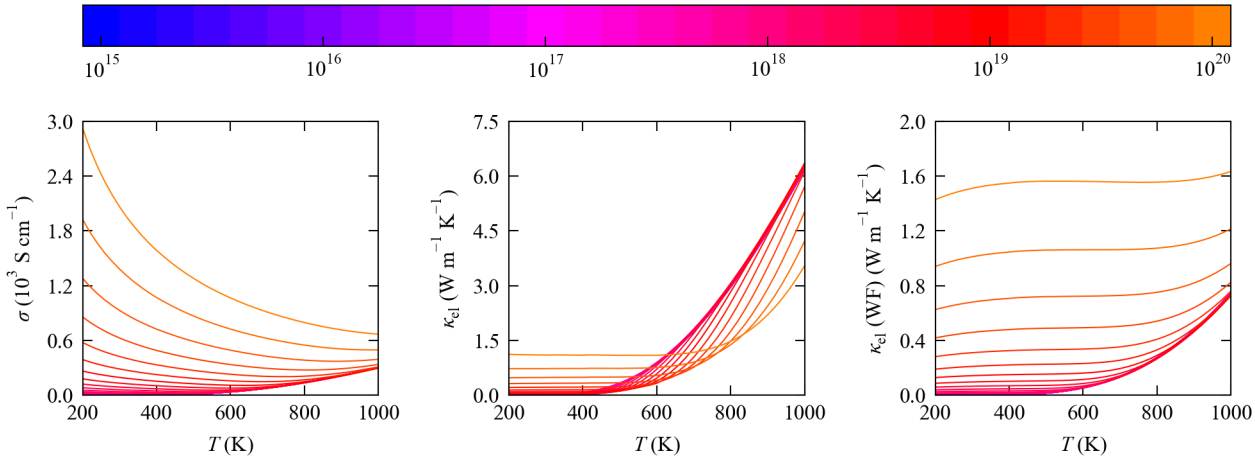

Figure S5. Comparison of the electrical conductivity σ of equilibrium rocksalt SnS with the electronic thermal conductivity κ_{el} computed using Eq. 7 in the manuscript and from the Weidemann-Franz law in Eq. 12. In each subplot the σ/κ_{el} are shown as a function of temperature for carrier concentrations n from 10^{15}-10^{20} cm^{-3}, denoted by line colours from blue (small n) to orange (large n).

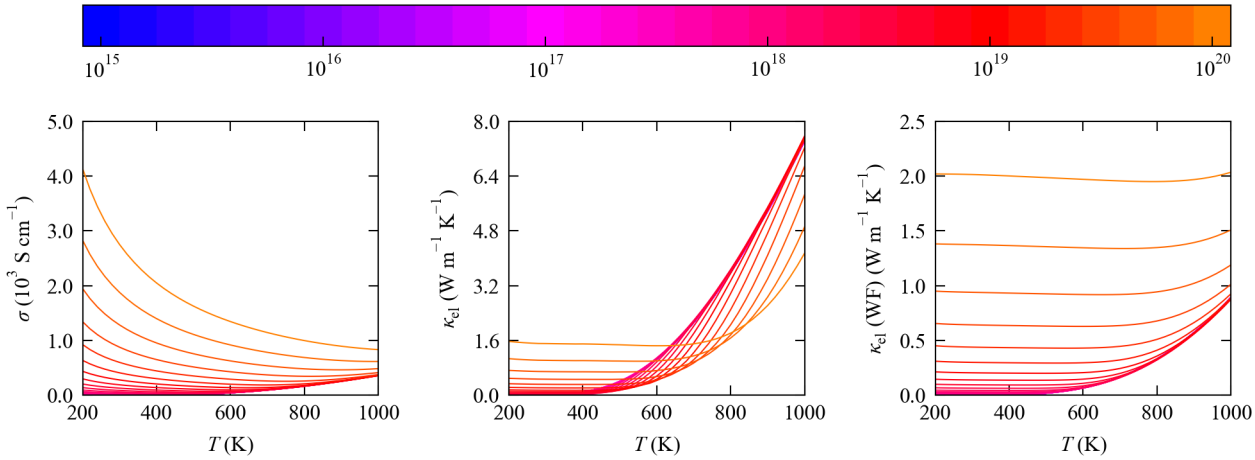

Figure S6. Comparison of the electrical conductivity σ of compressed rocksalt SnS with the electronic thermal conductivity κ_{el} computed using Eq. 7 in the manuscript and from the Weidemann-Franz law in Eq. 12. In each subplot the σ/κ_{el} are shown as a function of temperature for carrier concentrations n from 10^{15}-10^{20} cm^{-3}, denoted by line colours from blue (small n) to orange (large n).

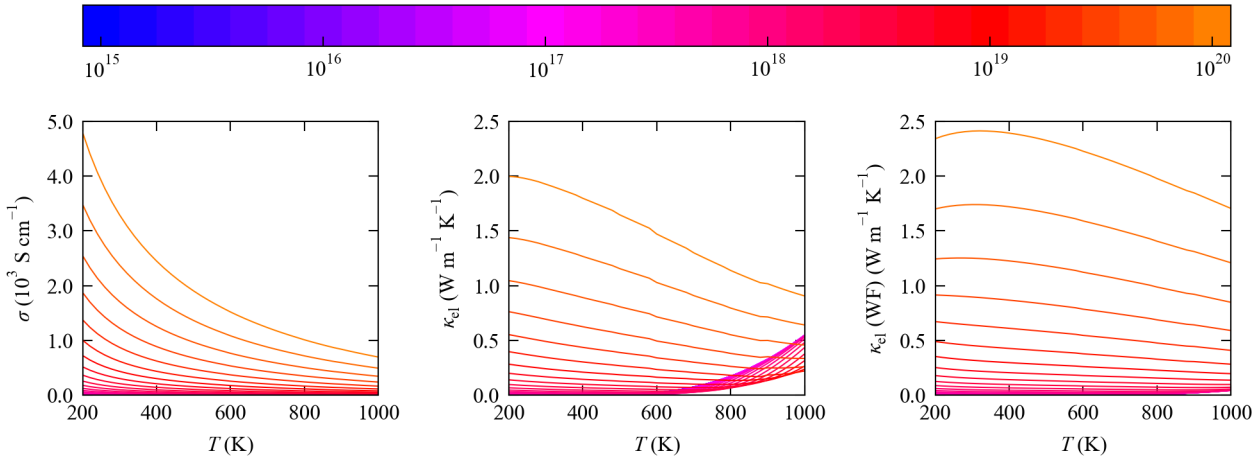

Figure S7. Comparison of the electrical conductivity σ of *Pnma* SnSe with the electronic thermal conductivity κ_{el} computed using Eq. 7 in the manuscript and from the Weidemann-Franz law in Eq. 12. In each subplot the σ/κ_{el} are shown as a function of temperature for carrier concentrations n from 10^{15}-10^{20} cm^{-3}, denoted by line colours from blue (small n) to orange (large n).

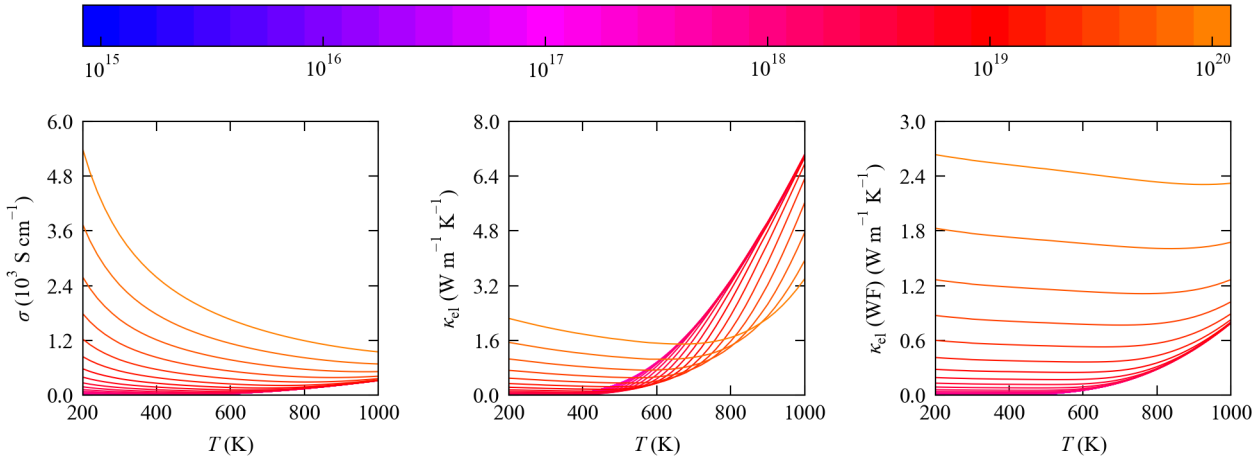

Figure S8. Comparison of the electrical conductivity σ of rocksalt SnSe with the electronic thermal conductivity κ_{el} computed using Eq. 7 in the manuscript and from the Weidemann-Franz law in Eq. 12. In each subplot the σ/κ_{el} are shown as a function of temperature for carrier concentrations n from 10^{15}-10^{20} cm^{-3}, denoted by line colours from blue (small n) to orange (large n).

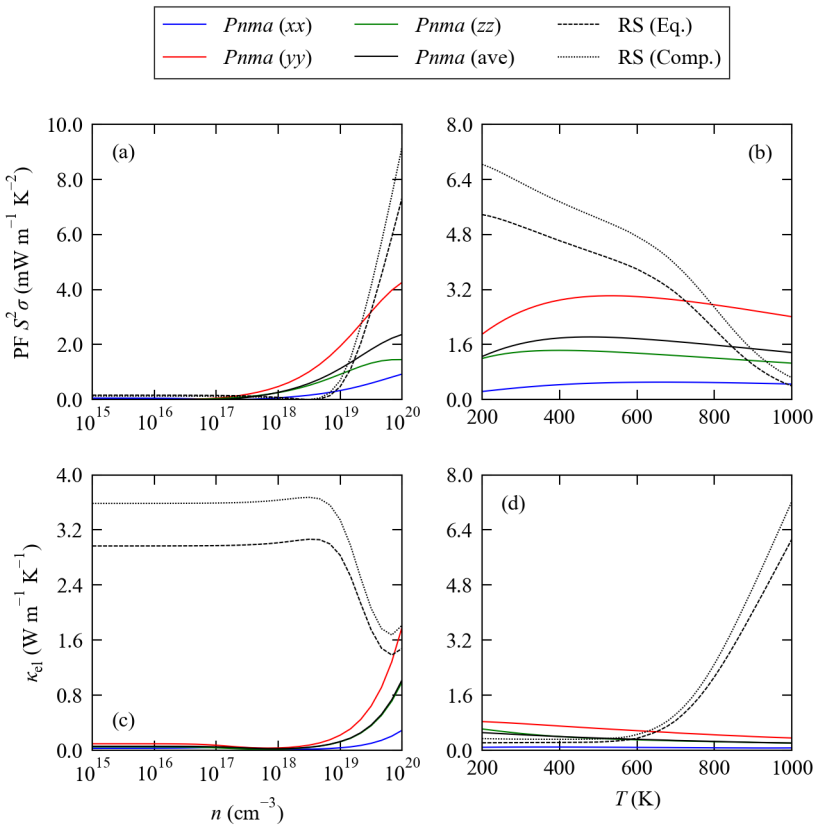

Figure S9. Anisotropy in the electronic transport of SnS. The plots show the diagonal xx, yy and zz components of the electrical conductivity σ (a/b), the Seebeck coefficient S (c/d), the power factor $S^2\sigma$ (PF; e/f) and electronic thermal conductivity κ_{el} (g/h) of orthorhombic (*Pnma*) SnS together with the isotropic averages calculated using Eqs. 9, 10 and 11 in the manuscript. The isotropic averages of the equilibrium and compressed rocksalt structures, for which the three diagonal components are equal, are also shown for comparison. All four properties are shown as a function of carrier concentration n for a fixed T = 800 K (a, c, e, g) and as a function of temperature for a fixed n = 2.15 × 10^{19} cm^{-3} (b, d, f, h).

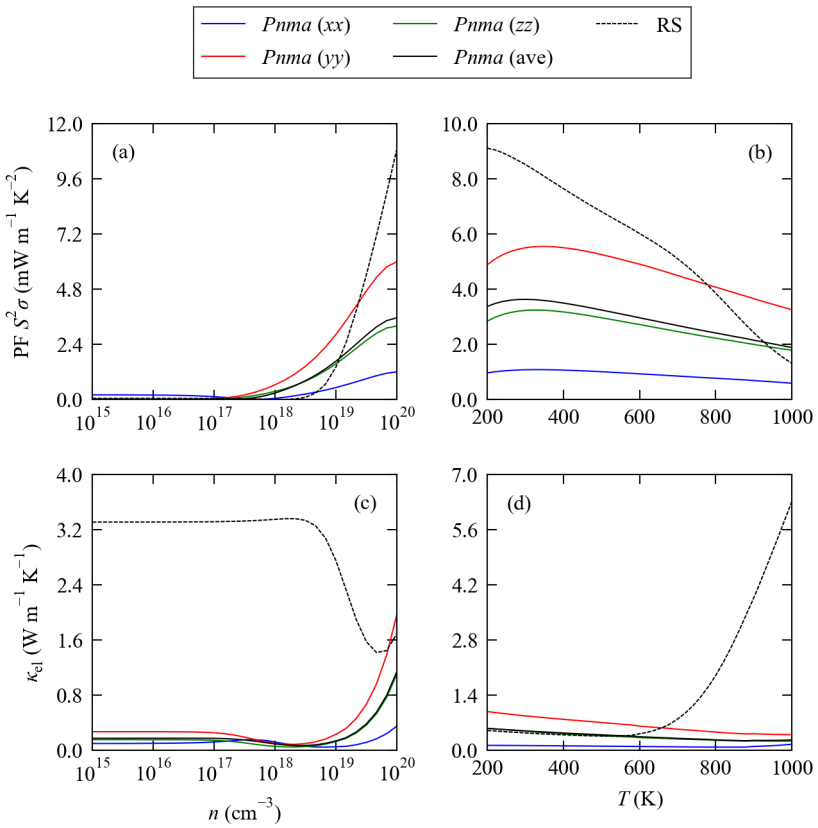

Figure S10. Anisotropy in the electronic transport of SnSe. The plots show the diagonal xx, yy and zz components of the electrical conductivity σ (a/b), the Seebeck coefficient S (c/d), the power factor $S^2\sigma$ (PF; e/f) and electronic thermal conductivity κ_{el} (g/h) of orthorhombic (*Pnma*) SnSe together with the isotropic averages calculated using Eqs. 9, 10 and 11 in the manuscript. The isotropic averages of the rocksalt phase, for which the three diagonal components are equal, are also shown for comparison. All four properties are shown as a function of carrier concentration n for a fixed T = 800 K (a, c, e, g) and as a function of temperature for a fixed $n = 2.15 \times 10^{19}$ cm^{-3} (b, d, f, h). The data in subplots (e/f) and (g/h) are the same as in Figure 4 in the manuscript.

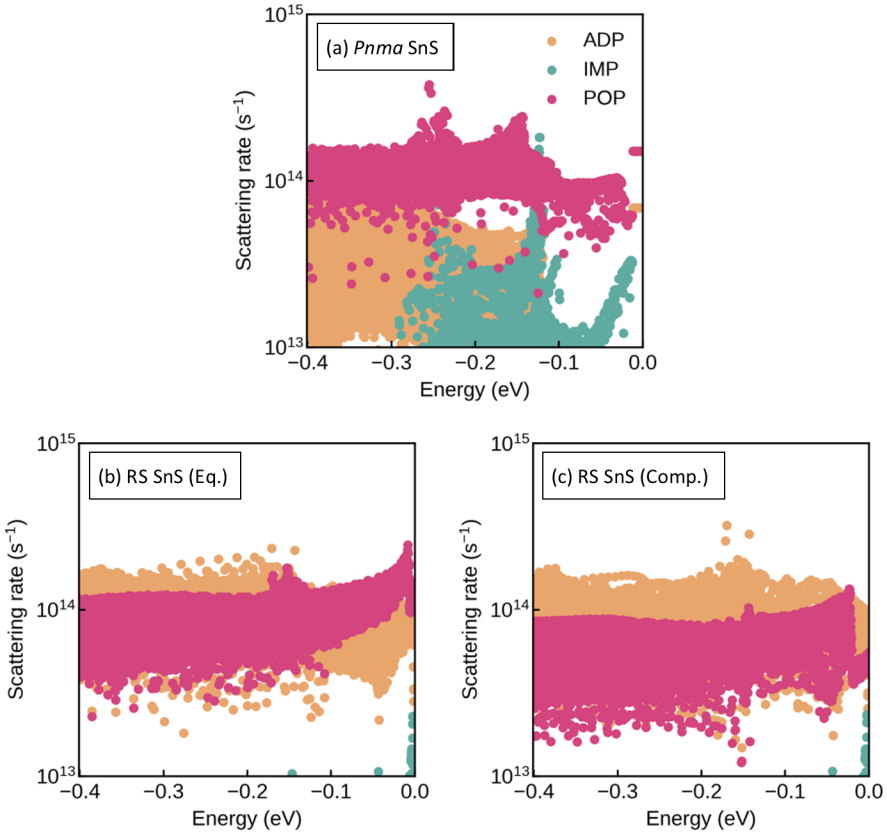

Figure S11. Calculated scattering rates τ_{kj}^{-1} as a function of energy ϵ_{kj} for the electronic states in *Pnma* (a) and equilibrium and compressed rocksalt SnS (RS; b/c) for a carrier concentration n = 2.15 $\times$ 10^{19} cm^{-3} and temperature T = 800 K. The energy zero is set to $\epsilon = \epsilon_{\mathrm{F}}$. Rates are shown separately for the three scattering mechanisms relevant to the three phases of SnS, namely acoustic deformation potential (ADP), polar optic phonon (POP) and ionised impurity (IMP) scattering.

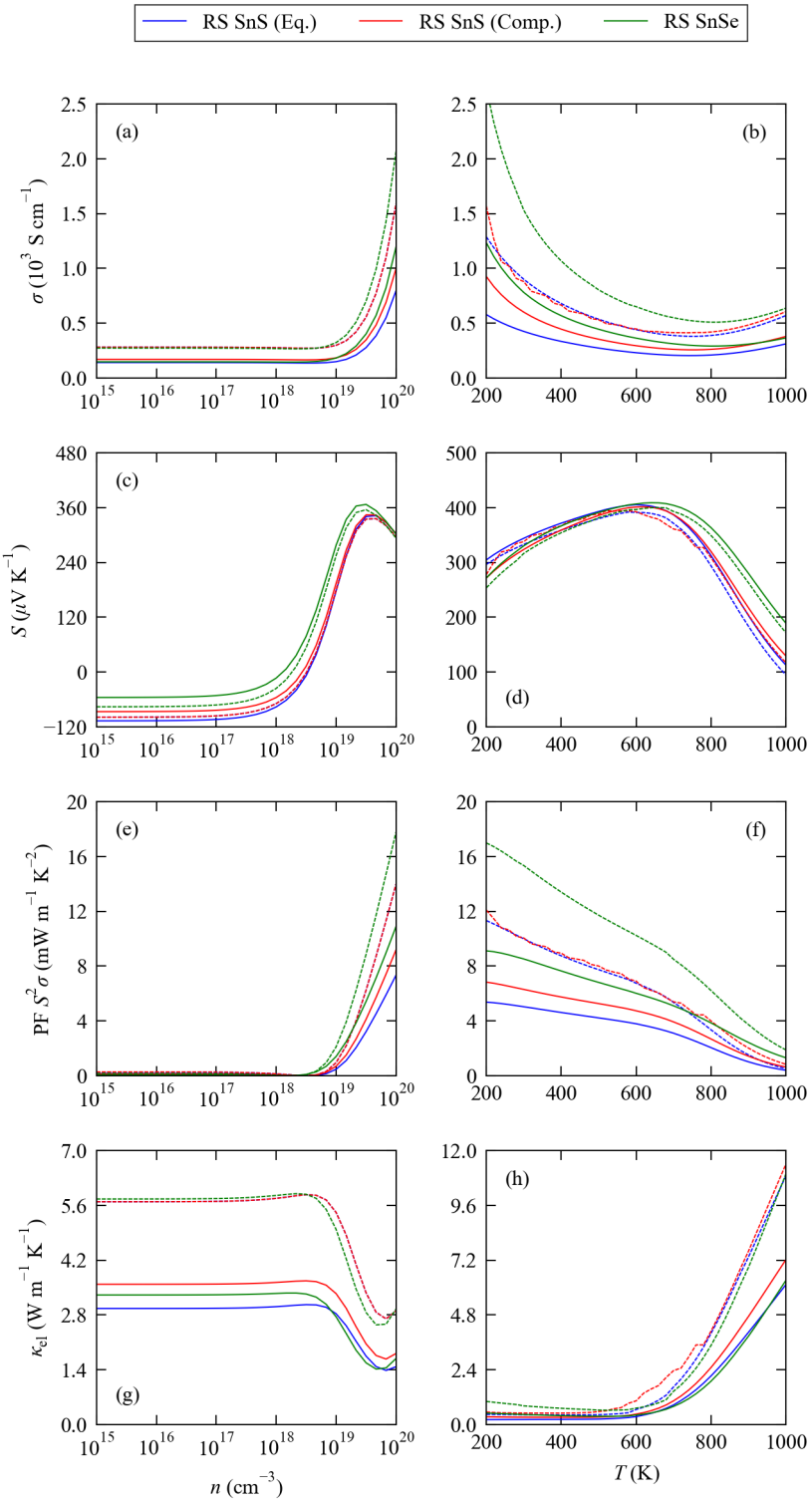

Figure S12. Comparison of the calculated electronic conductivity σ (a/b), Seebeck coefficient S (c/d), power factor $S^2\sigma$ (PF; e/f) and electronic thermal conductivity κ_{el} (g/h) of equilibrium and compressed rocksalt SnS and rocksalt SnSe computed with electron relaxation times determined from dielectric properties obtained using two different theoretical methods. The solid lines show the results from dielectric properties obtained with PBEsol + D3 [2,3] and density-functional perturbation theory (DFPT) to compute the high-frequency dielectric constant ε_∞.[4] This data is also plotted in Figure 3 in the manuscript. The dashed lines show properties determined with dielectric constants from the HSE 06 hybrid functional[5] using the finite-field method to compute the ε_∞.[6] The four properties are compared as a function of carrier concentration n for a fixed T = 800 K (a, c, e, g) and as a function of temperature for a fixed $n = 2.15 \times 10^{19}$ cm^{-3} (b, d, f, h).

References

1. Skelton, J.M. Approximate models for the lattice thermal conductivity of alloy thermoelectrics. *J. Mater. Chem. C* **2021**, *9*, 11772–11787. doi:10.1039/D1TC02026A.
2. Perdew, J.P.; Ruzsinszky, A.; Csonka, G.I.; Vydrov, O.A.; Scuseria, G.E.; Constantin, L.A.; Zhou, X.; Burke, K. Restoring the Density-Gradient Expansion for Exchange in Solids and Surfaces. *Phys. Rev. Lett.* **2008**, *100*, 136406. doi:10.1103/PhysRevLett.100.136406.
3. Grimme, S.; Antony, J.; Ehrlich, S.; Krieg, H. A consistent and accurate ab initio parametrization of density functional dispersion correction (DFT-D) for the 94 elements H-Pu. *J. Chem. Phys.* **2010**, *132*, 154104. doi:10.1063/1.3382344.
4. Gajdoš, M. and Hummer, K. and Kresse, G. and Furthmüller, J. and Bechstedt, F.. Linear optical properties in the projector-augmented wave methodology. *Phys. Rev. B* **2006**, *73*, 045112. doi:10.1103/PhysRevB.73.045112.
5. Krukau, A.V.; Vydrov, O.A.; Izmaylov, A.F.; Scuseria, G.E. Influence of the exchange screening parameter on the performance of screened hybrid functionals. *J. Chem. Phys.* **2006**, *125*, 224106. doi:10.1063/1.2404663.
6. Souza, Ivo and Íñiguez, Jorge and Vanderbilt, David. First-Principles Approach to Insulators in Finite Electric Fields. *Phys. Rev. Lett.* **2002**, *89*, 117602. doi:10.1103/PhysRevLett.89.117602.